Control of Bud Activation by an Auxin Transport Switch

Supporting Information

Przemyslaw Prusinkiewicz*, Scott Crawford, Richard S. Smith, Karin Ljung,
Tom Bennett, Veronica Ongaro, Ottoline Leyser*

*To whom correspondence should be addressed.
Email: pwp@cpsc.ucalgary.ca, hmol1@york.ac.uk

This file includes:

Materials and methods

All growth conditions, and all plant lines except those involving *tir3*, are as described in (*S1*) and (*S2*). Note that the *axr1-12* line described in (*S1*) was subsequently found to be *axr1-3*, as used in this study. The *tir3-101* line was obtained from the Nottingham Arabidopsis Stock Centre. The *tir3-101 max4-1* double mutant was generated by crossing the single mutants and then using the *tir3* dwarfism phenotype and the highly branched and basta resistance phenotypes conferred by the *max4-1* allele to identify the double mutant in the F2. Homozygosity for both mutations was confirmed in the F3.

Auxin analysis

Auxin collection: 2cm segments were excised from bolting stems of 6 week old plants. The stem segments were incubated for 24 hours with either their basal or apical ends in 50 µl 2.5mM diethyldithiocarbamate.

Auxin purification and quantitative analysis: 50 μl 0.05 M sodium phosphate buffer pH 7.0 containing 0.02% diethyldithiocarbamic acid (antioxidant), 500 pg $^{13}C_6$-IAA (internal standard) and 100 μl 1% acetic acid was added to each sample. The pH was adjusted to around 2.7 with 5 μl 1 M HCl before application of the sample to a 50-mg C18 BondElut SPE column (Varian, Middelburg, The Netherlands) conditioned with 1 ml of methanol and 1 ml of 1% acetic acid. The sample vial was rinsed with 100 μl 1% acetic acid that was also applied to the SPE column. The column was washed two times with 0.5 ml of 10% methanol in 1% acetic acid and then eluted two times with 0.5 ml of methanol. The combined sample was evaporated to dryness, dissolved in 0.2 ml of 2-propanol and 1 ml of dichloromethane, and methylated by adding 5 μL 2 M trimethylsilyl-diazomethane in hexane (Aldrich). It was then incubated at room temperature for 30 min. 5 μL of 2 M acetic acid in hexane was added to destroy excess diazomethane, and the sample was then evaporated to dryness. The methylated sample was trimethyl-silylated and analysed by gas chromatography–selected reaction monitoring–mass spectrometry as described in (*S3*).

PIN1p::PIN1:GFP imaging

Longitudinal hand sections of the bud stem were made. Sections were mounted in water and GFP fluorescence was immediately inspected. Images were taken using a Zeiss LSM 510 Meta NLO Multiphoton microscope equipped with a pulsed Ti:Sa IR Laser (Coherent Chameleon Ultra) exciting at 900 nm. A 40x water emersion (0.8NA) objective was used. Images were prepared using Zeiss LSM Image Browser Version 4.2.0.121.

Model implementation

All metamer-level simulations (Figures 1-4) and the associated plots (Figures S1 and S2) were specified in the L+C modeling language (*S4*, *S5*), which is based on the mathematical formalism of L-systems (*S6*, *S7*). At each stage of structure development, the differential equations comprising the model (Equations 2a and b, and Equation 11) were solved numerically using forward Euler's integration with time step $\Delta t = 0.05$. The adequacy of this scheme was verified by reducing the time step 10-fold; the same results were obtained. The simulations have been implemented and visualized using the software package L-studio (http://algorithmicbotany.org/lstudio).

The cellular-level simulation (Figure 5) has been based on an implementation of Mitchison's model (*S8*), re-written in the vv modeling environment (*S9*). The source code for all models is available on request.

Supporting text

Background information on the mathematical model of auxin transport and metamer polarization

The presented model has been designed to capture the essence rather than details of the bud activation mechanism, and thus has been constructed using several simplifying assumptions (see (*S10*, *S11*) for the methodological justification, and (*S12*) for a general discussion of the nature of assumptions underlying different approaches to the modeling of auxin-driven morphogenesis). The model is confined to a two-dimensional longitudinal section through the shoot (see (*S13*, *S14*) for examples of the same assumption applied to models of the shoot apical meristem, and (*S15*, *S16*), for examples applied to root models). Cells are abstracted as squares, arranged into a matrix (S8, *S17*, *S18*). The internal structure of cells is ignored, except for the distribution of PIN1 proteins, which are dynamically allocated to individual cell membranes (*S19*, *S20*, *S21*). Intercellular space is also ignored, and auxin exported from a cell *i* towards an adjacent cell *j* is assumed to enter the target cell directly (*S19*, *S20*, *S21*). In most simulations, the dynamics of auxin transport and PIN allocation are extended to entire apices, lateral buds and internodes (summarily referred to as metamers), which are treated as if they were individual cells; the validity of this extension is supported by a cell-level simulation. Additional assumptions are detailed in the text.

As outlined in the main paper, we assume that the auxin flux, i.e., the amount of auxin flowing through a unit surface in a unit time (*S22*), is given by the transport equation of the form

$$\Phi_{i\to j} = Tc_i\left[PIN_{i\to j}\right] - Tc_j\left[PIN_{j\to i}\right] + D\left(c_i - c_j\right). \qquad (1)$$

Here $\left[PIN_{i\to j}\right]$ is the surface concentration of PIN proteins directing auxin efflux from metamer *i* to metamer *j*, T characterizes the efficiency of PIN-dependent polar transport, and D is a coefficient of diffusion. We thus attribute polar auxin transport to the action of PIN proteins, and similar to (*S19*, *S23*), for example, assume that PIN-mediated membrane permeabilities are linear functions of PIN concentrations in the membranes. Furthermore, we assume that the concentrations $\left[PIN_{i\to j}\right]$ depend on flux, and change according to the equations:

$$\frac{d\left[PIN_{i\to j}\right]}{dt} = \rho_{i\to j}\frac{\Phi_{i\to j}^n}{K^n + \Phi_{i\to j}^n} + \rho_0 - \mu\left[PIN_{i\to j}\right] \qquad \text{if } \Phi_{i\to j} \geq 0, \qquad (2a)$$

$$\frac{d\left[PIN_{i\to j}\right]}{dt} = \rho_0 - \mu\left[PIN_{i\to j}\right] \qquad \text{if } \Phi_{i\to j} < 0, \qquad (2b)$$

where $\rho_{i\to j}$ is the maximum rate of auxin flux-driven PIN allocation to the membrane of cell *i* facing cell *j*, ρ_0 is the basal (flux-independent) rate of PIN allocation, and μ is the decay constant capturing the rate with which PINs leave the membrane spontaneously. PIN allocation is described by a Hill function (*S24*) with coefficients *K* and *n*. Analogous equations describe dynamics of PIN allocation to the opposite membrane:

$$\frac{d[PIN_{j\to i}]}{dt} = \rho_{j\to i}\frac{\Phi_{j\to i}^n}{K^n + \Phi_{j\to i}^n} + \rho_0 - \mu[PIN_{j\to i}] \qquad \text{if } \Phi_{j\to i} \geq 0, \tag{3a}$$

$$\frac{d[PIN_{j\to i}]}{dt} = \rho_0 - \mu[PIN_{j\to i}] \qquad \text{if } \Phi_{j\to i} < 0. \tag{3b}$$

For $\rho_{i\to j} = \rho_{j\to i}$, the equation system 1-3 closely resembles Mitchison's model of flux-dependent auxin transport (*S18*, Equations 10), see also (*S8*, Equation 4). The difference is the use of the Hill function (first term on the right side of Equation 3a) instead of the quadratic function considered in detail by Mitchison (who observed, however, that a sigmoidal function is generally needed (*S17*), see also (*S23*)). The use of the Hill function makes it possible to simulate saturating dependence of PIN allocation on auxin flux, which – as revealed by the following analysis – is essential to the operation of our model.

Qualitative analysis of the transport and polarization model

Equations 1-3 describe a dynamic system, the state of which is characterized by three variables: $\Phi_{i\to j} = -\Phi_{j\to i}$, $[PIN_{i\to j}]$, and $[PIN_{j\to i}]$. To analyze this system, we eliminate the variables $[PIN_{i\to j}]$ and $[PIN_{j\to i}]$ and focus on the flux $\Phi_{i\to j}$. To this end, we differentiate Equation (1) assuming that the values other than fluxes and PIN concentrations are constant or are changing comparatively slowly (c.f. (*S19*, *S21*)), and thus their derivatives can be neglected:

$$\frac{d\Phi_{i\to j}}{dt} = Tc_i\frac{d[PIN_{i\to j}]}{dt} - Tc_j\frac{d[PIN_{j\to i}]}{dt}. \tag{4}$$

Considering the case $\Phi_{i\to j} \geq 0$ first, we substitute the right sides of Equations 2a and 3b for the rates of change $d[PIN_{i\to j}]/dt$ and $d[PIN_{j\to i}]/dt$ in the resulting Equation 4:

$$\frac{d\Phi_{i\to j}}{dt} = Tc_i\rho_{i\to j}\frac{\Phi_{i\to j}^n}{K^n + \Phi_{i\to j}^n} + Tc_i\rho_0 - Tc_i\mu[PIN_{i\to j}] - Tc_j\rho_0 + Tc_j\mu[PIN_{j\to i}]. \tag{5}$$

We then use a transformed Equation (1),

$$Tc_i\left[PIN_{i\to j}\right]-Tc_j\left[PIN_{j\to j}\right]=\Phi_{i\to j}-D\left(c_i-c_j\right), \tag{6}$$

to eliminate terms $Tc_i\left[PIN_{i\to j}\right]$ and $Tc_j\left[PIN_{j\to i}\right]$ in Equation (5):

$$\frac{d\Phi_{i\to j}}{dt}=\rho_{i\to j}Tc_i\frac{\Phi_{i\to j}}{K^n+\Phi_{i\to j}}-\mu\Phi_{i\to j}+\left(\mu D+\rho_0 T\right)\left(c_i-c_j\right). \tag{7a}$$

For $\Phi_{i\to j}=-\Phi_{j\to i}<0$ we compute, in a similar manner,

$$\frac{d\Phi_{j\to i}}{dt}=\rho_{j\to i}Tc_j\frac{\Phi_{j\to i}}{K^n+\Phi_{j\to i}}-\mu\Phi_{j\to i}+\left(\mu D+\rho_0 T\right)\left(c_j-c_i\right), \tag{7b}$$

and, by substituting $-\Phi_{i\to j}$ for $\Phi_{j\to i}$, we obtain

$$\frac{d\Phi_{i\to j}}{dt}=-\rho_{j\to i}Tc_j\frac{\left(-\Phi_{i\to j}\right)^n}{K^n+\left(-\Phi_{i\to j}\right)^n}-\mu\Phi_{i\to j}+\left(\mu D+\rho_0 T\right)\left(c_i-c_j\right). \tag{7c}$$

Equations 7a and c describe self-enhancing auxin transport between any pair of adjacent cells that obey the canalization model. Specializing these equations for plant stems, we assume that the rate of auxin flux-driven PIN allocation is positive for basipetal fluxes, but equal to zero for acropetal fluxes, $\rho_{i\to j}=\rho>0$ and $\rho_{j\to i}=0$. This brings Equations 7a and c to their final form:

$$\frac{d\Phi_{i\to j}}{dt}=\rho Tc_i\frac{\Phi_{i\to j}^n}{K^n+\Phi_{i\to j}^n}-\mu\Phi_{i\to j}^n+\left(\mu D+\rho_0 T\right)\left(c_i-c_j\right) \qquad \text{if } \Phi_{i\to j}\geq 0, \tag{8a}$$

$$\frac{d\Phi_{i\to j}}{dt}=-\mu\Phi_{i\to j}+\left(\mu D+\rho_0 T\right)\left(c_i-c_j\right) \qquad \text{if } \Phi_{i\to j}<0. \tag{8b}$$

From a biological perspective, the above assumption of asymmetry in PIN polarization is justified by the experimental evidence for the established basipetal polarity of auxin transport in the stem (*S25, S26*). While our model produces similar patterns of bud activation in non-polarized stems as well, we use this assumption to simplify the mathematical analysis of the model.

The key properties of the dynamical system represented by Equations 8 are revealed by its qualitative analysis. For a positive source auxin concentration, $c_i>0$, Equation 8a represents a sigmoidal curve (first term on the right-hand side of this equation, Figure S1A, see Table S1 for parameter values). This curve is sheared (second term, Figure S1B) and translated in the direction of the y axis (third term, Figure S1C) by an amount proportional to the auxin concentration at the sink, c_j. The x-intercepts of the resulting

curve indicate system equilibria (since the flux $\Phi_{i\to j}$ does not change when $d\Phi_{i\to j}/dt = 0$) for the given sink auxin concentration c_j. Each equilibrium is stable when the slope of the curve at the intersection point is negative and unstable when the slope is positive (*S27*). Positions of equilibria for different sink concentrations c_j are summarily presented in the bifurcation diagram (Figure S1D). When the sink concentration c_j is low (e.g., $c_j = 5$), there is a single stable equilibrium state representing high auxin flux from the source to the target metamer. In contrast, when the concentration c_j is high (e.g., $c_j = 10$), there are two stable equilibria, corresponding to either low or high auxin flux. The presence of these stable equilibria indicates that the actual flux value and the corresponding PIN concentration at the face of the source metamer depend on the history of the system.

To model and analyze this behavior in the context of a branching plant structure, we complement the model of membrane behavior (Equations 8) with the balance law (*S22*), which relates fluxes to auxin concentrations:

$$\frac{dm_i}{dt} = \sum_j \Phi_{j\to i} A_{i,j} + \left[\sigma_i (H - c_i) - \nu c_i\right] V_i . \tag{9}$$

Here m_i denotes the mass of auxin in metamer i, $\Phi_{j\to i}$ is the auxin influx ($\Phi_{j\to i} \geq 0$) or efflux ($\Phi_{j\to i} < 0$) through the face separating metamers i and j, and $A_{i,j}$ is the area of this face. Furthermore, coefficients σ_i and ν control the rates of auxin production and turnover, H is the target concentration if the cell is a source of auxin (i.e., $\sigma_i > 0$), c_i is the current concentration, and V_i is the volume of metamer i. The term $\sigma_i(H - c_i)$ models auxin production in a manner asymptotically approaching a target level, according to a widely used generic formula (*S24*). We assume that auxin is only produced in apices (both terminal and lateral). When an apex switches from the vegetative to flowering state, its target auxin concentration decreases from a high value H to a residual value H_r, and/or rate of auxin production σ_i decreases from a high value σ to a residual rate σ_r.

The auxin concentration c_i and mass m_i in metamer i are related to each other by the metamer volume: $c_i = m_i / V_i$. We use this relation to eliminate mass from Equation 9:

$$\begin{aligned} \frac{dc_i}{dt} &= \frac{1}{V_i^2}\left(\frac{dm_i}{dt} V_i - m_i \frac{dV_i}{dt}\right) = \frac{1}{V_i}\frac{dm_i}{dt} - c_i \frac{1}{V_i}\frac{dV_i}{dt} \\ &= \frac{1}{V_i}\sum_j \Phi_{j\to i} A_{i,j} + \sigma_i (H - c_i) - \nu c_i - c_i \cdot RERG_{V_i} \end{aligned} \tag{10}$$

The symbol $RERG_{V_i}$ denotes the relative elementary rate of growth (*S28*, *S29)* in volume of metamer i, and captures the decrease in auxin concentration due to the metamer expansion. Although not used explicitly in our model, this term indicates that rapid stem

elongation at bolting reduces auxin concentration in the stem and thus contributes to the lifting of apical dominance and lateral bud activation in nature.

Given an arbitrary assembly of M cells or metamers sharing N faces, the system of M coupled equations of form 11 and $2N$ equations of form 8 a and b models changes in auxin concentrations and fluxes over time. The dynamics of this system in a simple branching structure are illustrated in Figure S2. The extension of these dynamics to a shoot explains the patterns of bud activation presented in the main text.

The model of shoot growth

In the developmental models (Figures 2-4), the shoot apex periodically adds new metamers (internodes with their associated lateral buds) to the shoot axis. The plastochron has been set to 1 time unit. With the time step $\Delta t = 0.05$ used for the numerical integration of Equations 2a, 2b and 10 there are thus 20 simulation steps per plastochron. The development of the shoot axis ends when the apex switches from the vegetative to flowering state. The switch is controlled by a variable called vegetativeness (*S30*). Initially set to a high value, the vegetativeness decreases over time and switches the terminal apex from vegetative to flowering state when it drops below a predefined threshold. The switch to flowering also reduces the rate of auxin production in the apex. The resulting decrease in auxin concentration propagates basipetally along the main stem, triggering auxin efflux from the lateral buds through a relay mechanism described in the main text. A lateral bud becomes active (i.e., switches state from dormant to vegetative state) when the auxin efflux from the bud exceeds a predefined threshold, Φ_{th}. An active bud creates a lateral axis in a process similar to the creation of the main axis by the terminal apex. Simulation parameters for shoot development have been chosen such that the vegetative main apex produces 8 metamers before the switch to flowering, and an active lateral apex produces 2 metamers.

Parameter values

Although estimates for the values of some parameters used in our simulations exist (e.g. (*S12*, *S14*, *S16*, *S19*)), other values, in particular those pertinent to the dynamics of auxin-driven PIN polarization, are not yet known. Consequently, we chose to use dimensionless parameters in our simulations. This is consistent with our emphasis on the qualitative nature of the switching mechanism inherent in the canalization model. Similar simulation results can be obtained for a wide range of parameter values: with some coordination between different parameters, most parameters can be significantly changed – even by several orders of magnitude – while qualitatively preserving the simulation results (not shown). Furthermore, our model is not sensitive to the exact form of equations, as long as the sigmoidal relation between auxin flux and the rate of its change (Figure S1) is preserved. The values in Table S1 are thus reported to assure reproducibility of our results, rather than estimate the physical values.

Table S1. Parameter values used in simulations. Simulations are divided into three groups. Within each group, all simulations use the same parameter values except when shown otherwise.

Parameter		Simulation group												
		1			2									3
Name	Sym-bol	S1A	S1 B-D	S2, 1B-F	2D-F acro-petal	2G-H *axr3*, repl.	2I over-comp.	3A-E w.t.	3F con-verg.	4A *axr1*	5D *max4*	5E *tir3*	5F *max4 tir3*	5B-F cell-level
Polar transport coefficient	T	0.5				0.2		0.5						2
Diffusion coefficient	D	0.1						0.02						2
PIN allocation rate	$\rho_{i\to j}$	7.5						10				5	5	0.17
Hill exponent	n	3						3						3
Hill saturation coefficient	K	1.3						0.5						10
Base PIN production rate	ρ_0	0						0.15						.15
PIN turnover rate	μ	0	10	10				7.5			2.5		2.5	0.1 a)
Target auxin concentration	H	N/A		10				10		14				10
Residual auxin concentration	H_r	N/A		3.0		10	10	2.5						10
Auxin production rate	σ	N/A		10				10						10
Residual auxin production rate	σ_r	N/A		10				10						0.08
Auxin turnover rate	ν	N/A		0.1	0.2			0.005	0.03					0.08
Auxin turnover in the root	ν_{root}	N/A		1.0				1.0						N/A b)
Metamer/cell volume	V_i	N/A		1.0				1.0						1.0
Face area	$A_{i,j}$	N/A		1.0				1.0						1.0
Threshold bud-activation flux	Φ_{th}	N/A						2.0						N/A
Simulation time step	Δt	N/A		0.05				0.05						0.05
Frames shown		N/A	N/A	c)	0, 50, 130	175, 275 d)	238 d)	0, 70, 225, 400, 1500	485	2000	2000 e)	2000	2000	450, 6750, 13500, 22500, 38250

a) After reaching the value of 1.0, surface PIN concentration cannot drop below 1.0.
b) Auxin concentration in the basal cell is fixed at 0.
c) Simulation controlled interactively.
d) Plant decapitated interactively after simulation step 175
e) PIN concentration visualized at a scale reduced by 1/3 w.r.t. the other simulations.

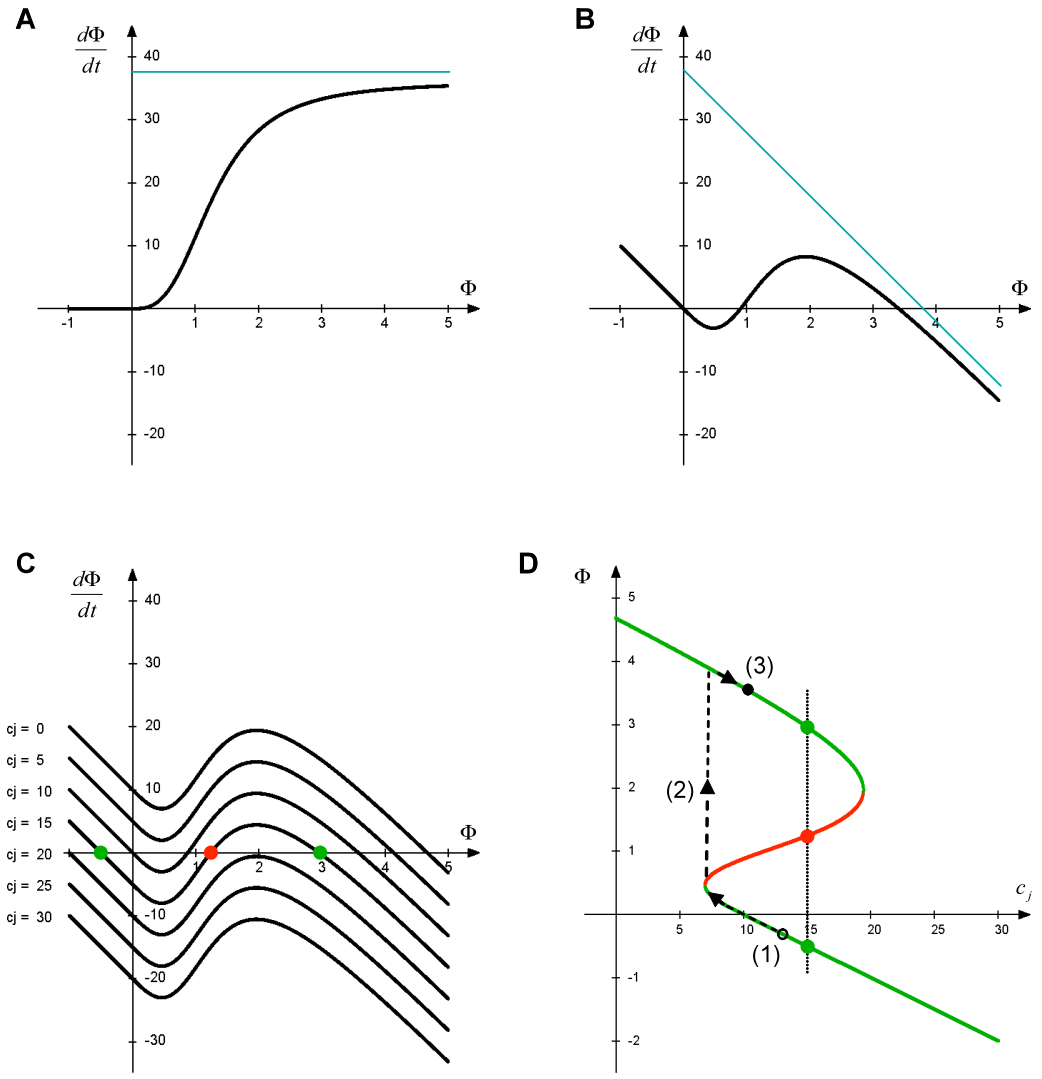

Figure S1. Qualitative analysis of the dynamical system described by Equations 8. Parameter values are given in Table S1; all plots have been drawn assuming source auxin concentration c_j = 10. **(A-C)** Graphical interpretation of the Equations 8. (A) A sigmoidal curve described by the term $\rho T c_i \Phi^n / \left(K^n + \Phi^n\right)$ for $\Phi \geq 0$ and 0 for $\Phi < 0$. (B) The sheared curve obtained by subtracting the term $\mu\Phi$ from the term depicted in (A). The blue lines in (A) and (B) are the asymptotes for $\Phi \to \infty$. (C) The family of curves resulting from the addition of the term $\left(\mu D + \rho_0 T\right)\left(c_i - c_j\right)$, for different auxin concentrations in the sink c_j, to the curve (B). Green dots show stable equilibria, and the red dot shows the unstable equilibrium for the sample concentration c_j = 15. (D) Bifurcation diagram, showing positions of equilibria as a function of sink concentration c_j. Green and red dots indicate these equilibria for the concentration c_j = 15, corresponding to (C). The entire diagram (hysteresis curve) was obtained by plotting positions of stable and unstable equilibria for values c_j ranging from 0 to 30. Black arrows and dashed lines indicate a sample progression of states of a face between a source and a sink, which occurs when the sink auxin concentration c_j first decreases, then increases: flux Φ jumps (line 2) from the initial small value (open black circle 1) to the large final value (closed black circle 3). This progression is at the heart of the switch of the lateral bud from the dormant to active state, cf. Fig. S2 B-D.

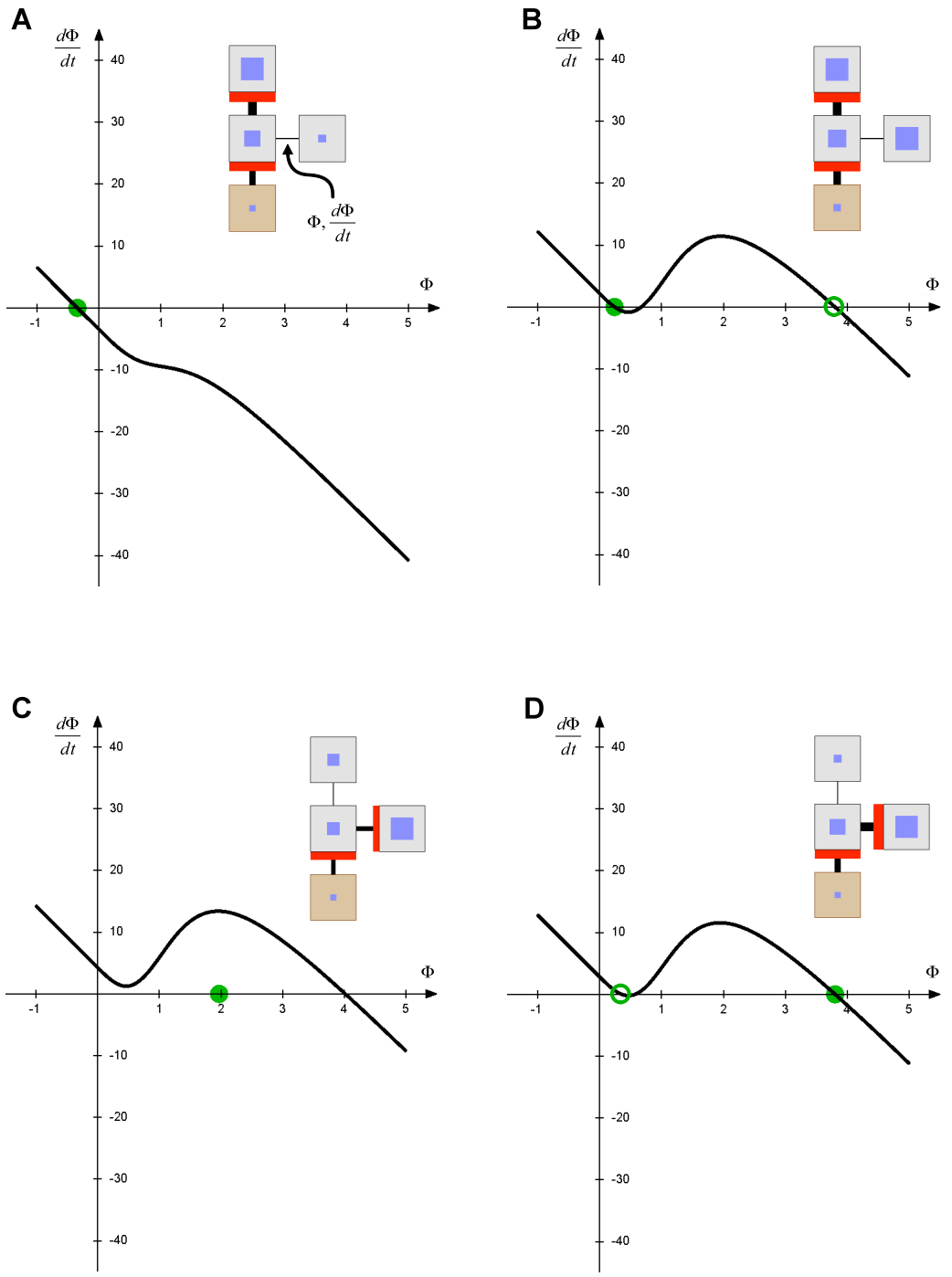

Figure S2. Typical progression of patterns of auxin transport in a branching structure from Figure 1, simulated using a canalization model (Equations 1, 2, and 10). The modeled structure (insets) is the same as in Figure 1. Plots associated with each structure show the rate of change of auxin efflux from the lateral bud, $d\Phi / dt$, as a function of the efflux Φ from this bud (Equations 8a,b). The filled green circle indicates current flux Φ. The simulation was driven by a user, who interactively increased auxin production in the lateral bud between stages A and B, then decreased auxin production in the terminal metamer between stages B and C. (**A**) The initial state: Auxin originating in the terminal metamer is transported through the branching node to the

sink. There is a small negative flux from the branching node to the lateral bud due to diffusion and/or residual amounts of PIN proteins present in all faces. (**B**) Local auxin production has been increased, augmenting auxin concentration in the bud. A second stable state emerges (open green circle), but auxin efflux from the bud remains low due to the continuous progression from state A to B. (**C**) Auxin production in the terminal metamer has been decreased, leading to reduced auxin concentration in the branching node. The function plot shifts upward, making the previous stable state disappear. As a result, flux Φ jumps towards the remaining stable state, characterized by high auxin efflux from the lateral bud. (**D**) Auxin supply from the lateral bud increases auxin concentration in the branching node. The first stable state reappears (open green circle), but efflux from the lateral bud remains high. The path of auxin influx into the branching node has thus switched from the terminal to the lateral metamer, reflecting the history of the system. The progression of states depicted in Figures (B) to (D) corresponds to the progression of states (1)-(3) in Figure S1D.

Supporting references

S1. Bennett T et al (2006) The *Arabidopsis MAX* pathway controls shoot branching by regulating auxin transport. *Curr Biol* 16:553-563.

S2. Ongaro V, Bainbridge K, Williamson L, Leyser O (2008) Interactions between axillary branches of Arabidopsis. *Mol Plant* 1:388-400

S3. Edlund A, Eklöf S, Sundberg B, Moritz T, Sandberg G (1995) A microscale technique for gas chromatography-mass spectrometry measurements of picogram amounts of indole-3-acetic acid in plant tissue. *Plant Physiol* 108:1043-1047.

S4. Karwowski R, Prusinkiewicz P (2003) Design and implementation of the L+C modeling language. *ENTCS* 86(2):134-152.

S5. Prusinkiewicz P, Karwowski R, Lane B (2007) The L+C plant modeling language. In *Functional-Structural Plant Modeling in Crop Production*, eds Vos J et al. (Springer, Dordrecht), chap 3.

S6. Lindenmayer A (1968) Mathematical models for cellular interaction in development, Part I and II. *J Theor Biol* 18:280-315.

S7. Prusinkiewicz P, Lindenmayer A (1990), *The Algorithmic Beauty of Plants* (Springer, New York).

S8. Rolland-Lagan AG, Prusinkiewicz P (1995) Reviewing models of auxin canalization in the context of leaf vein pattern formation in Arabidopsis. *Plant J* 44:854-865.

S9. Smith C, Prusinkiewicz P, Samavati F (2003) Local specification of surface subdivision algorithms. *LNCS* 3062:313-327.

S10. Gaines B (1977) System identification, approximation, and complexity. *Int J Gen Syst* 3:147-177.

S11. Bak P (1996) *How Nature Works. The Science of Self-Organized Criticality* (Copernicus/Springer, New York), pp 41-45.

S12. Kramer EM (2008) Computer models of auxin transport: a review and commentary. *J Exp Bot* 59:45-53.

S13. Stoma S et al. (2008) Flux-based transport enhancement as a plausible unifying mechanism for auxin transport in meristem development. *PLoS Comput Biol* 4(10): e1000207, doi:10.1371/journal.pcbi.1000207.

S14. Bayer EM et al. (2009) Integration of transport-based models for phyllotaxis and midvein formation. *Genes Dev* 23:373-384.

S15. Swarup R et al. (2005) Root gravitropism requires lateral root cap and epidermal cells for transport and response to a mobile auxin signal. *Nature Cell Biol.* **7**:1057-1065.

S16. Grieneisen VA, Xu J, Maree AF, Hogeweg P, Scheres B (2007) Auxin transport is sufficient to generate a maximum and gradient guiding root growth. *Nature* 449:1008-1013.

S17. Mitchison GJ (1980) A model for vein formation in higher plants. *Proc R Soc Lond B* 207:79-109.

S18. Mitchison GJ (1981) The polar transport of auxin and vein patterns in plants. *Philos Trans R Soc Lond B* 295:461-471

S19. Jönsson H, Heisler MG., Shapiro BE, Meyerowitz EM, Mjolsness E (2006). An auxin-driven polarized transport model for phyllotaxis. *Proc Natl Acad Sci* USA 103:1633-1638.

S20. Barbier de Reuille P et al (2006) Computer simulations reveal properties of the cell-cell signalling network at the shoot apex in *Arabidopsis*. *Proc Natl Acad Sci* USA 103:1627-1632.
S21. Smith RS et al (2006) A plausible model for phyllotaxis. *Proc Natl Acad Sci* USA 103:1301-1306.
S22. Edelstein-Keshet L (1988) *Mathematical Models in Biology* (Random House, New York), p 394.
S23. Feugier F, Mochizuki A, Iwasa Y (2005) Self-organization of the vascular system in plant leaves: Inter-dependent dynamics of auxin flux and carrier proteins. *J Theor Biol* 236:366-375
S24. Alon U (2007) *An Introduction to Systems Biology* (Chapman/CRC, Boca Raton), pp 13,19.
S25. Sachs T (1991) *Pattern Formation in Plant Tissues* (Cambridge Univ. Press, Cambridge), chap 5.
S26. Sheldrake AR (1974) The Polarity of auxin transport in inverted cuttings. *New Phytol*. 73: 637-642
S27. Hale J, Koçak H (1991) *Dynamics and Bifurcations* (Springer, New York), p 18.
S28. Richards O, Kavanagh A (1943) The analysis of the relative growth gradients and changing form of growing organisms: Illustrated by the tobacco leaf. *Am. Nat.* 77: 385-399.
S29. Hejnowicz Z, Romberger J (1984). Growth tensor of plant organs. *J Theor Biol* 110:93-114.
S30. Prusinkiewicz P, Erasmus Y, Lane B, Harder L, Coen E (2007) Evolution and development of inflorescence architectures. *Science* 316:1452-1456.

Description of animations

Animation S1 (corresponds to Figure S2). Typical progression of auxin transport at a branching node. Simulation was controlled interactively, by first increasing auxin production in the lateral bud, then decreasing production in the terminal bud. The dynamic plot characterizes auxin efflux from the lateral bud.

Animation S2 (corresponds to Figure 2D-F). Simulation of acropetal bud activation

Animation S3 (corresponds to Figure 2G-H). Simulation of a decapitation experiment in the *axr3* mutant. Removal of the shoot apical meristem activates the lateral bud immediately below the decapitation site.

Animation S4 (corresponds to Figure 2I). Simulation of a decapitation experiment with overcompensation. Removal of the shoot apical meristem activates the two lateral buds closest to the decapitation site.

Animation S5 (corresponds to Figure 3A-E). Basipetal propagation of bud activation as found in wild-type Arabidopsis. The cascade of bud activation stops at three lateral buds due to residual auxin production after floral transition.

Animation S6. Unlimited basipetal propagation of bud activation. Simulation parameters are the same as in Animation S5 except for the residual auxin production, which is set to 0.

Animation S7 (corresponds to Figure 3F). Simulation of a convergent activation pattern.

Animation S8 (corresponds to Figure 4A). Simulation of bud activation in the *axr1* mutant.

Animation S9 (corresponds to Figure 5D). Simulation of bud activation in the *max4* mutant.

Animation S10 (corresponds to Figure 5E). Simulation of bud activation in the *tir3* mutant.

Animation S11 (corresponds to Figure 5F). Simulation of bud activation in the double *max4,tir3* mutant.

Animation S12 (corresponds to Figure 5B-F). Simulation of bud activation at the cellular level.